HHS Public Access

Author manuscript

J Med Chem. Author manuscript; available in PMC 2016 August 25.

Published in final edited form as:

J Med Chem. 2016 May 12; 59(9): 4210–4220. doi:10.1021/acs.jmedchem.5b01146.

Structure-Based Inhibitor Design for Evaluation of a CYP3A4 Pharmacophore Model

Parminder Kaur[†,‖], **A. Richard Chamberlin**[†,‡], **Thomas L. Poulos**[†,‡,§], and **Irina F. Sevrioukova**[*,§]

[†]Department of Pharmaceutical Sciences, University of California—Irvine, Irvine, California 92697, United States

[‡]Department of Chemistry, University of California—Irvine, Irvine, California 92697, United States

[§]Department of Molecular Biology and Biochemistry, University of California—Irvine, Irvine, California 92697, United States

Abstract

Human cytochrome P450 3A4 (CYP3A4) is a key xenobiotic-metabolizing enzyme that oxidizes and clears the majority of drugs. CYP3A4 inhibition may lead to drug–drug interactions, toxicity, and other adverse effects but, in some cases, could be beneficial and enhance therapeutic efficiency of coadministered pharmaceuticals that are metabolized by CYP3A4. On the basis of our investigations of analogs of ritonavir, a potent CYP3A4 inactivator and pharmacoenhancer, we have built a pharmacophore model for a CYP3A4-specific inhibitor. This study is the first attempt to test this model using a set of rationally designed compounds. The functional and structural data presented here agree well with the proposed pharmacophore. In particular, we confirmed the importance of a flexible backbone, the H-bond donor/acceptor moiety, and aromaticity of the side group analogous to Phe-2 of ritonavir and demonstrated the leading role of hydrophobic interactions at the sites adjacent to the heme and phenylalanine cluster in the ligand binding process. The X-ray structures of CYP3A4 bound to the rationally designed inhibitors provide deeper insights into the mechanism of the CYP3A4–ligand interaction. Most importantly, two of our compounds (**15a** and **15b**) that are less complex than ritonavir have comparable submicromolar affinity and inhibitory potency for CYP3A4 and, thus, could serve as templates for synthesis of second generation inhibitors for further evaluation and optimization of the pharmacophore model.

[*]**Corresponding Author** sevrioui@uci.edu. Phone: (949) 824-1953.

[‖]**Present Address** P.K.: William Paterson University, 300 Pompton Road, Wayne, NJ 07470.

ASSOCIATED CONTENT

Supporting Information

The Supporting Information is available free of charge on the ACS Publications website at DOI: 10.1021/acs.jmed-chem.5b01146.

X-ray data collection and refinement statistics and mass spectrometry and NMR data for compounds **4–15a,b** (PDF)

Molecular formula strings (CSV)

Accession Codes

PDB codes for **4**-, imidazole/**4**-, **15a**-, and **15b**-bound CYP3A4 have been deposited in the Protein Data Bank and are the following, respectively: 4D75, 4D6Z, 4D78, and 4D7D.

The authors declare no competing financial interest.

Graphical Abstract

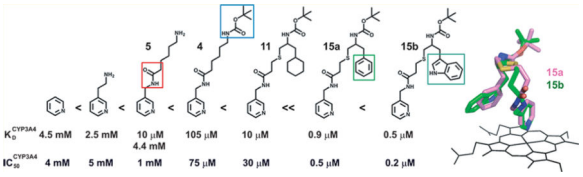

INTRODUCTION

Cytochrome P450 3A4 (CYP3A4) is the most abundant and clinically relevant xenobiotic-metabolizing enzyme in humans. CYP3A4 catalyzes diverse oxidative reactions and is involved in the metabolism of endogenous steroids, the majority of administered drugs, and other foreign molecules, such as environmental pollutants, carcinogens, pesticides, and insecticides.[1–8] CYP3A4 has a large and malleable active site that accommodates a wide variety of molecules, some of which could inhibit or enhance metabolism. In vivo, CYP3A4 inhibition has a greater impact on human health, as it can lead to xenobiotic-induced toxicity and drug–drug interactions, one of the reasons for late-stage clinical trial failures and withdrawal of marketed pharmaceuticals.

However, carefully controlled CYP3A4 inhibition can be beneficial and is currently exploited in the treatment of HIV infection. To date, two CYP3A4 inhibitors, ritonavir and cobicistat (Figure 1), are marketed as pharmacoenhancers for the HIV-I protease inhibitors that serve as substrates for CYP3A4.[9–13] Both drugs were developed based on chemical structure–activity relationships studies rather than the CYP3A4 crystal structure. Moreover, ritonavir was originally designed to inhibit the HIV-1 protease,[14] whereas its ability to potently inactivate CYP3A4 was coincidental and discovered later.[9] Cobicistat is a derivative of ritonavir that lacks the backbone hydroxyl group, critical for binding to catalytic Asp25 and Asp225 of HIV-1 protease, and has a morpholine ring instead of the valine side group (Figure 1). As a result, cobicistat is not an anti-HIV protease inhibitor, so its prolonged usage does not promote the development of drug-resistant HIV strains. Also, this pharmaceutical has fewer side effects and better physicochemical properties, yet is comparable but not superior to ritonavir in terms of inhibitory potency for CYP3A4.[12]

There is no general agreement on the CYP3A4 inhibitory mechanism of ritonavir. Several groups suggested that ritonavir is a mechanism-based inactivator,[15–19] whereas others argued against the mechanism-based CYP3A4 inhibition[20] and concluded that ritonavir acts as a competitive[21] or a mixed competitive–noncompetitive CYP3A4 inactivator.[22–24] Our data on highly purified recombinant CYP3A4 do not support the mechanism-based or competitive type of inhibition as a predominant inactivation pathway and rather suggest that ritonavir inactivates CYP3A4 via strong thiazole nitrogen coordination to both ferric and ferrous CYP3A4 which decreases the heme redox potential and impedes electron transfer from the redox partner, cytochrome P450 reductase.[25] This conclusion is well supported by the X-ray structures of CYP3A4 complexed with ritonavir and 10 ritonavir analogs.[25–28] Most importantly, the accumulated functional and structural data enabled us to identify several important trends in the ligand binding process and define strategies for rational,

structure-based inhibitor design.[29] In particular, we found that (i) strong binding through the heme-ligating moiety is a prerequisite for potent CYP3A4 inhibition, and pyridine possesses more favorable stereoelectronic properties for the heme ligation than any other chemical group tested; (ii) the flexible backbone enables a better fit into the CYP3A4 active site; (iii) the side group at a Phe-2 position (indicated in Figure 1) is critically important because it not only fills the hydrophobic cavity (P2 site) but also has a potential to stabilize the protein–ligand complex via different types of interactions with the heme-ligating group and nearby Arg105; (iv) occupation of the pocket hosting the Phe-1 group (P1 site) is also important and greatly improves inhibitory potency; (v) polar interactions with Ser119 increase ligand affinity and association rate, regardless of whether the hydrogen bond with the ligand is established or not; (vi) the terminal group modulates the CYP3A4-inhibitor complex affinity and stability, which in turn correlate with the ligand-induced changes in the melting temperature and the amplitude of the 442 nm absorption of the ferrous ligand-bound form.

Previous 3D pharmacophores for drug metabolism prediction were built based on P450 homology and quantitative structure–activity relationship (QSAR) modeling because the X-ray structure of CYP3A4 was not available at that time.[30–33] In addition, there is no structure-based inhibitor pharmacophore that could assist in identification and early elimination of potential CYP3A4 inactivators during development of drugs and other chemicals relevant to public health. Having mapped the inhibitory determinants within the CYP3A4 active site, we were able to build a pharmacophore model for a CYP3A4-specific inhibitor (Figure 2).[29] Our strategy for the model evaluation was to synthesize and analyze ritonavir-like molecules using a general scaffold (Figure 3) where the pyridine ring serves as a heme-ligating moiety and the remainder of the inhibitor is stitched together with units containing various side and terminal groups (R_1–R_3). By systematically changing R_1–R_3 substituents, it can be probed how each chemical moiety contributes to the binding affinity and inhibitory potency and how CYP3A4 adapts to changes in the ligand's structure.

Here we present structural and functional results on the first set of commercially available and rationally designed pyridine-containing compounds that differ in the backbone length and R_2 substituents (Figure 4). With this initial set, we were able to confirm the importance of a flexible backbone, aromaticity of the R_2 group, and the H-bond donor/acceptor moiety (pharmacophoric determinants II, III, and V), as well as the leading role of hydrophobic interactions at the P1 and P2 sites in the ligand binding process.

RESULTS AND DISCUSSION

Inhibitor Design

As mentioned in the **Introduction**, both CYP3A4 inhibitors currently marketed as pharmacoenhancers, ritonavir and cobicistat (Figure 1), were developed based on chemical structure–activity relationships studies rather than the CYP3A4 crystal structure. Ritonavir is a large peptidomimetic drug designed to inhibit an HIV-I protease,[9] whereas cobicistat was developed through ritonavir derivatization.[13,34] Synthesis of both compounds is a complex process requiring production of specific stereoisomers. To evaluate our pharmacophore

model, we decided to build CYP3A4 inhibitors from scratch using a general simple scaffold (Figure 3) where the modules containing the side and terminal groups (R_1, R_2, and R_3) are linked to the heme-ligating pyridine via a flexible backbone. Pyridine and aminoethylpyridine (Figure 4) were obtained from Sigma-Alrdrich. The rationale for designing compounds **4**, **5**, **11**, and **15a,b** was to determine how elongation of the backbone, introduction of the H-bond donor/acceptor (peptide bond), and substitution of R_2 affect affinity, inhibitory potency, and the ligand binding mode. Mass spectrometry and NMR data for compounds **4**–**15a,b** are included in the Supporting Information.

Binding Affinity and Association Kinetics

Addition of pyridine, aminoethylpyridine, and compound **5** to CYP3A4 led to a decrease and a small red shift (~2 nm) in the Soret band (Figure 5). Spectral dissociation constants (K_s) for pyridine and aminoethylpyridine were in the millimolar range (Table 1), whereas **5** had two binding sites with K_s of 10 μM and 4.4 mM. Compounds **4, 11**, and **15a,b**, on the other hand, bind to a single site and induce a notable shift in the Soret band, typical for type II ligands (Figure 6). Introduction of the hexane or phenyl side group increased the binding affinity by 10- and 100-fold, respectively, relative to **4**. The phenyl-to-indole substitution led to a further decline in K_s (by ~2-fold, Table 1). Another important feature is a pronounced 442 nm absorption of the ferrous **15a**- and **15b**-bound forms of CYP3A4. The corresponding 442 nm peak was considerably smaller for the CYP3A4-4/ **11** complexes and undetectable for the pyridine-, aminoethylpyridine-, and **5**-bound forms (Figures 5 and 6). In our previous studies,[25–28] we found that the amplitude of the 442 nm band of the ferrous species correlates with the inhibitory potency of the ligand, in that compounds whose binding led to a higher 442 nm absorption peak were acting as more potent CYP3A4 inactivators (e.g., ritonavir and pyridine-substituted desoxyrito-navir (GS3; Figure 1)). Therefore, a significant but not complete conversion to the 442 nm absorbing species taking place upon association of CYP3A4 with **15a** and **15b** was the first indication that these compounds may have a comparable although not superior inhibitory potency relative to GS3 and ritonavir.

The binding reactions of CYP3A4 with pyridine, aminoethylpyridine, and **5** were monophasic, with rate constants of 0.5–0.8 s^{-1}. In contrast, association with **4, 11**, and **15a,b** proceeded in two phases. The rate constant for the fast phase (k_{fast}) was the highest for **4** and the lowest for **15a** (20 and 1.7 s^{-1}, respectively; Table 1). Notably, k_{fast} for **15a** was close to that of ritonavir (1.4 s^{-1})[25] and nearly 5-fold lower than the respective value for **15b** and GS3. Together, the spectral and kinetic data suggest that (i) the backbone elongation and addition of a side group complicate the binding reaction, (ii) the presence of a bulky, hydrophobic R_2 group increases the ligand affinity but slows down the association rate, and (iii) indole as a R_2 substituent promotes complex formation with CYP3A4 to a higher degree than the hexane or phenyl rings.

Melting Temperature and Inhibitory Potency

None of the investigated compounds increased the thermal stability of CYP3A4, as evidenced by the lack of feasible ligand-dependent changes in melting temperature (ΔT_m; Table 1). CYP3A4 T_m was slightly increased upon complex formation with **15b** but decreased in the presence of other compounds, most notably for the **11**- and **15a**-bound

forms (by 1–2 °C). This is in contrast to ritonavir and its analogs, whose ligation to CYP3A4 increases T_m by 2–7 °C.[27,28] Nevertheless, a common trend revealed by thermal denaturation is an increase in thermostability of CYP3A4 upon association with ritonavir-like compounds. The heme ligation and occupation of the P1 and P2 cavities by hydrophobic moieties likely stabilize CYP3A4 by decreasing conformational flexibility.

As expected, the inhibitory potency of the investigated compounds on the BFC debenzylation activity of CYP3A4 correlated with the binding affinity (Table 1). The IC_{50} values were the highest for pyridine, aminoethylpyridine, and **5** (1–4 mM), intermediate for **4** and **11** (75 and 30 μM, respectively) and the lowest for **15a** and **15b** (0.5 and 0.2 μM, respectively). Importantly, IC_{50} values for **15a** and **15b** were close to those for ritonavir and GS3 (0.55 and 0.13 μM, respectively).[27] Thus, addition of only one aromatic side group and tert-butyloxy-carbonyl (Boc) as a terminal moiety transforms compound **5**, a very weak ligand, into a potent CYP3A4 inactivator.

Crystal Structures of the 15a–and 15b–BoundCYP3A4

We succeeded in cocrystallization of CYP3A4 with **4, 15a**, and **15b**. Compound **11** dissociated from CYP3A4 during crystallization. Crystal structures of CYP3A4 ligated to **15a** and **15b** were determined to 2.60 and 2.76 Å, respectively (Supporting Information Table 1S). Both compounds bind to the active site and ligate to the heme iron through the pyridine nitrogen (Figure 7). The GS3-bound model (PDB code 4I4H) was used for comparative analysis because this analog is most similar to the investigated compounds. Superposition of the **15a**-, **15b**-, and GS3-bound structures reveals that **15a** and **15b** rotate around the pyridine nitrogen by ~180° (Figure 7C) to place the phenyl/indole rings between the heme-ligating pyridine and Arg105 guanidinium group (P2 site), right where the Phe-2 side group of GS3 is positioned. Most strikingly, the terminal Boc groups are in a similar position and displace Phe304 and the I-helix to the same extent as Phe-1 of GS3 does (Figure 7D). Since the phenyl and indole moieties are oriented differently from GS3 Phe-2, which is nearly parallel to the pyridine and Arg105 guanidine groups and closer to the heme plane, the **15a,b** conformations are less optimal for hydrophobic, π–π, and π–cation interactions with the heme, pyridine, and the Arg105 guanidine, respectively. Another important dissimilarity that may decrease affinity of **15a,b** is that their binding mode disallows H-bonding with Ser119 (Figure 7C). Nevertheless, the comparable K_s and IC_{50} values for **15b** and GS3 imply that the larger and more electron-rich indole ring may partially compensate for the less favorable orientation by establishing new or more extensive van der Waals contacts with the neighboring Arg105, Ala370, heme, and pyridine.

Modification of Surface Residues in CYP3A4 for Improvement of Crystal Diffraction

Wild type CYP3A4 willingly cocrystallizes with **4**, but similar to other ligand-bound forms, diffraction data of this complex did not exceed 2.5 Å. At this resolution, electron density for **4** was discontinuous and the ligand association mode could not be accurately determined. To overcome this problem, we decided to introduce surface mutations that help form intermolecular contacts in the crystal lattice and improve X-ray diffraction power without affecting the CYP3A4 ligand binding and metabolism. Using a surface entropy reduction prediction (SERp) server (http://services.mbi.ucla.edu/SER/),[35] several surface peptides

containing clusters of bulky charged residues (Arg, Lys, and/or Glu) were identified (Table 2). One cluster with a high score, Lys282/Glu283/ Glu285, is part of the surface loop that is disordered in all crystal structures reported to date. We mutated this site and found a variant, K282A/E285A, that was better expressed in *E. coli*, associated with **4** similar to the wild type, and produced crystals with lower mosaicity and higher diffraction power. This mutant was used for determination of the CYP3A4–**4** complex structure.

Crystal Structures of the CYP3A4-4 Complexes

Cocrystals of CYP3A4 K282A/E285A with **4** were grown under two different conditions that led to two distinct modes of ligand binding. The first complex was crystallized in the presence of imidazole and contained both compound **4** and imidazole in the active site (Figure 8A). In this structure, determined to 1.93 Å, imidazole ligates to the heme iron and **4** binds nearby. Such a ligand arrangement is stabilized by two hydrogen bonds formed between the carbonyl oxygen and amide nitrogen of **4** and the imidazole nitrogen and the Ser119 hydroxyl group, respectively. The pyridine moiety of **4** is adjacent but not embedded into the P1 pocket. Through hydrophobic interactions with Phe108, Phe213, Phe215, and Phe340 (Figure 8B), the pyridine ring reinforces the phenylalanine cluster, a unique feature of CYP3A4.[36] The aliphatic linker of **4** forms van der Waals contacts with the Arg105 side chain, whereas the Boc group is placed at the P2 site and forms hydrophobic and van der Waals interactions with the Ile369-Ala370 peptide and the Arg212 side chain. Thus, when the space near the heme iron is occupied, the flexible compound **4** adopts a conformation that allows H-bonding to Ser119 and optimizes hydrophobic interactions mediated by the Boc and pyridine moieties. It is not clear though why the pyridine of **4** does not insert into the P1 pocket as Boc of **15a–b** (Figure 7D) and Phe-2 of GS3 and other ritonavir analogs do (Figure 8C).[25,27,28] The observed orientation may be preferable because it prevents steric clashing with Phe304 and the I-helix displacement. Alternatively, insertion into the P1 cavity may require some force (e.g., a push), which the flexible core of nonligated **4** cannot provide.

The X-ray structure of the CYP3A4-4 complex formed in the absence of imidazole was determined to 2.25 Å. In this structure, **4** is directly ligated to the heme iron via the pyridine nitrogen and, similar to **15a,b**, rotates by ~180° relative to GS3 (Figure 9). The flexible linker bends to allow the end portion to occupy the P2 site. This and the lack of H-bonds between **4** and the protein suggest once again that hydrophobic interactions, especially at the P2 site, are dominant and define the ligand binding mode.

CONCLUSIONS

The data obtained with the first set of rationally designed compounds support the proposed pharmacophore model for a CYP3A4-specific inhibitor and emphasize the importance of pharmacophoric determinants II, III, and V (Figure 3), as well as the dominant role of hydrophobic forces at the P1 and P2 sites during the ligand-binding process. In particular, with this initial set, we were able to confirm that (i) the flexible backbone enables ligands to better fit into the CYP3A4 active site and optimize interactions mediated by the side and terminal moieties; (ii) the P2 site is occupied by ligands first, and interactions at this site are

dominant and define the overall ligand binding mode; (iii) the P1 cavity is the second preferable site that ligands tend to occupy, even if it leads to the I-helix distortion; and (iv) H-bonding interactions with Ser119 are established when possible to stabilize the CYP3A4-ligand complex.

There were also new findings that provided additional insights into the ligand binding process. First, pyridine and its short-chain aliphatic derivative, aminoethylpyridine (Figure 4), were found to be very weak CYP3A4 inactivators (Table 1). This means that ligation of the pyridine nitrogen to the heme iron is weak and dissociable but becomes strong and virtually irreversible when the pyridine ring becomes part of the larger ligands, especially those capable of occupying the P2 and P1 sites. Second, based on the K_s and IC_{50} values for **11, 15a**, and **15b** (Table 1) and the inability of **11** to cocrystallize with CYP3A4, we conclude that aromaticity rather than hydrophobicity of the R_2 substituent is the key feature that stabilizes the protein–ligand complex and drastically improves affinity and inhibitory potency. Third, the structural data demonstrate that the P1 site can be occupied by the terminal group if R_1 is absent. That none of the R_1-lacking compounds markedly affected CYP3A4 T_m suggests, however, that Boc-mediated interactions at the P1 site are suboptimal and cannot provide the binding energy on the same scale as phenyl substituents of R_1 do (e.g., in ritonavir and GS3). Fourth, there was no correlation between ΔT_m and IC_{50} for the investigated compounds (Table 1), but as observed for other ritonavir analogs,[27,28] the inhibitory potency was proportional to the 442 nm absorption of the ferrous ligand-bound species. Thus, during ligand screening, the latter parameter may predict strong CYP3A4 inactivators more reliably than ΔT_m. Finally, two of the rationally designed compounds, **15a** and **15b**, are less structurally complex than GS3 and ritonavir but inhibit CYP3A4 with a comparable, submicromolar potency. This raises the possibility that simpler and more potent CYP3A4 inactivators than ritonavir can be designed through **15a,b** optimization.

EXPERIMENTAL PROCEDURES

Synthesis of Analogs

Synthesis of Compound 2—Di-*tert*-butyloxycarbonyl, $(Boc)_2O$ (1.99g, 9.14 mmol) was added to a solution of 6-aminohexanoic acid (1g, 7.61 mmol) and NaOH (10% aqueous solution) in 1,4-dioxane. The reaction mixture was then stirred overnight at room temperature. The solvent was evaporated and the mixture was acidified using 1 N HCl. The acidified mixture was then extracted with dichloromethane (DCM). The organic layer was washed with brine, dried over Na_2SO_4, filtered, and concentrated. The crude material was then purified using column chromatography to give the pure product **2** (1.57g, 89%).

Synthesis of Compounds 4 and 5 (Scheme 1)—Compound **2** (1g, 4.23 mmol) was added to a solution of EDAC (1.67g, 10.80 mmol) in dimethylformamide (DMF). The mixture was stirred at room temperature for 30 min after which DIPEA (3.76 mL, 21.61 mmol) and 3-(aminomethyl)pyridine **3** (0.70g, 6.34 mmol) were added to the reaction mixture. The reaction was allowed to stir for 16 h. On completion, the solvent was evaporated and the reaction mixture was diluted with ethyl acetate. The organic layer was then washed with saturated $NaHCO_3$, water, and brine. The combined organic layer was

dried over Na_2SO_4 and concentrated to give the crude product which was then purified using column chromatography (ethyl acetate/ methanol). The pure product **4** was obtained as white solid in 65% yield (0.91g). ^{1}H NMR ($CDCl_3$, 500 MHz) δ 8.53 (s, 2H), 7.64 (*d*, *J* = 7.82 Hz, 1H), 7.27 (t, *J* = 4.80 Hz, 1H), 5.95 (bs, 1H), 4.56 (bs, 1H), 4.46 (d, *J* = 5.91 Hz, 2H), 3.10 (q, *J* = 6.45 Hz, 2H), 2.23 (t, *J* = 7.45 Hz, 2H), 1.68 (quin, *J* = 7.5 Hz, 2H), 1.50–1.46 (m, 2H), 1.42 (s, 9H), 1.34 (m, 2H); ^{13}C NMR ($CDCl_3$, 125 MHz) δ 149.1, 148.8, 135.8, 123.7, 41.0, 36.4, 29.8, 28.4, 26.3, 25.2. HRMS *m/z* calculated for $C_{17}H_{27}N_3O_3$ $[M + Na]^+$: 344.21. Found: 344.2.

Compound **4** (0.6 g, 1.86 mmol) was treated with trifluoroacetic acid in DCM for 14 h at room temperature in order to remove the Boc group. The completion of the reaction was monitored through TLC. The reaction solvent was evaporated and the crude product was passed through Celite to obtain the pure amine **5** (0.47 g, 78% yield). ^{1}H NMR (500 MHz, CD_3OD) δ 8.81 (1H, s), 8.79–8.78 (2H, d, *J* = 5.5 Hz), 8.53–8.51 (1H, d, *J* = 8.3 Hz), 8.06–8.03 (1H, m), 2.97–2.91 (2H, m), 2.37–2.34 (2H, t, *J* = 7.4 Hz), 1.72–1.68 (4H, m), 1.48–1.39 (4H, m); ^{13}C NMR (CD_3OD, 125 MHz) δ 175.2, 161.1, 144.5, 142.4, 139.2, 126.4, 39.7, 38.9, 34.3, 29.8, 26.6, 24.3. HRMS *m/z* calculated for $C_{12}H_{19}N_3O$ $[M + H]^+$: 222.23. Found: 222.2.

After optimizing different conditions and routes, we started synthesis of the first generation analogs using (*S*)-Boc-phenylalaninol as shown in Scheme 2 and Scheme 3. (*S*)-Boc-phenylalaninol or other corresponding amino alcohols (shown in the schemes) were converted to a tosylate using *p*-toluenesulfonyl chloride, which was then reacted with 3-mercaptopro-pionic acid in the presence of NaOH at 50 °C to give the corresponding acid. The acid was then coupled to the 2-(3-pyridyl)ethylamine using the known usual EDAC coupling to give the corresponding final product.

Synthesis of Compound 7—(*S*)-Boc-phenylalaninol (2 g, 7.96 mmol) was dissolved in methanol and treated with rhodium on charcoal (5%, 100 mg) under H_2 atmosphere overnight to reduce the phenyl ring. The solution was then passed through Celite plug, and methanol was evaporated to give the pure product **7** in quantitative yield (2.01g, quant).

Synthesis of Compound 8—(*S*)-*Boc*-cyclohexylalaninol (2 g, 7.78 mmol) was dissolved in DCM. To this solution, triethylamine (3.25 mL, 23.34 mmol) and *p*-toluenesulfonyl chloride (2.23 g, 11.67 mmol) were added slowly at 0 °C. The reaction was then allowed to stir at room temperature overnight. After reaction completion, DCM was evaporated and the crude reaction mixture was purified using column chromatography. The pure product **8** was obtained as white fluffy solid (2.3 g, 71% yield). LCMS *m/z* calculated for $C_{21}H_{33}NO_5S$ $[M + Na]^+$: 434.21. Found: 434.23.

Synthesis of Compound 10—To solution of compound **8** (1 g, 2.43 mmol) in DMF, 3-mercaptopropanoic acid **9** (0.309 g, 2.91 mmol) was added. To this mixture, 1 N NaOH (2 mL) was added, and reaction was allowed to stir for 5 h at 50 °C. The crude product **10** was obtained by evaporating the solvent and was used for the next step without any further purification due to instability of the product on silica column. LCMS *m/z* calculated for $C_{17}H_{31}NO_4S$ $[M + 2Na]^+$: 368.20. Found: 368.17.

Synthesis of Compound 11—Compound **10** (0.1 g, 0.3 mmol) was added to a solution of EDAC (0.12 g, 0.72 mmol) in DMF. The mixture was stirred at room temperature for 30 min after which DIPEA (0.23 mL, 1.45 mmol) and 3-(aminomethyl)pyridine **3** (0.042 g, 0.43 mmol) were added. The reaction was allowed to stir for 18 h. On completion, the solvent was evaporated and the reaction mixture was diluted with ethyl acetate. The organic layer was then washed with saturated $NaHCO_3$, water, and brine. The combined organic layers were dried over Na_2SO_4 and concentrated to give the crude product which was then purified using column chromatography (ethyl acetate/methanol). The pure product **11** was obtained as yellow oil in 22% yield (0.005 g). ^{1}H NMR (400 MHz, CD_2C1_2) δ 9.31–9.07 (1H, m), 8.56 (2H, bs), 7.70–7.57 (2H, m), 7.33 (1H, bs), 4.54 (1H, s), 3.74–3.20 (5H, m), 3.14–3.04 (6H, m), 2.43–2.26 (1H, m), 1.67–1.51 (4H, m), 1.44–1.33 (2H, m), 1.26 (8H, s), 1.17–1.11 (3H, m), 1.04 (3H, m). ^{13}C NMR (100 MHz, CD_2C1_2) δ 132.6, 130.5, 64.4, 32.0, 31.6, 29.9, 29.3, 27.0, 24.7, 23.4, 22.9, 22.5, 15.4, 15.2, 14.6, 13.8, 12.8, 12.0. LCMS *m/z* calculated for $C_{23}H_{37}N_3O_3S$ $[M + Na]^+$: 458.22. Found: 458.21.

General Procedure for Synthesis of Compounds 15a and 15b

Synthesis of Compound 13a: (*S*)-Boc-phenylalaninol (lg, 3.98 mmol) was dissolved in DCM. To this solution, triethylamine and *p*-toluenesulphonyl chloride were added slowly at 0 °C. The reaction was then allowed to stir at room temperature overnight. After reaction completion, DCM was evaporated and the crude reaction mixture was purified using column chromatography. The pure product **13a** was obtained as white fluffy solid in 78% yield (1.26 g). The pure product **13b** was obtained as white solid in 81% yield.

Synthesis of Compound 14a—To the solution of compound **13a** (0.5 g, 1.23 mmol) in DMF, 3-mercaptopropanoic acid **9** (0.157 g, 1.48 mmol) was added. To this mixture, 1 N NaOH (2 mL) was added, and reaction was allowed to stir at 50 °C for 5 h. The crude product **14a** was obtained by evaporating the solvent and was used for the next step without any further purification. LCMS *m/z* calculated for **14a:** $C_{17}H_{25}NO_4S$ $[M + Na]^+$: 362.15. Found: 362.17. LCMS *m/z* calculated for **14b:** $C_{19}H_{26}N_2O_4S$ $[M - H^+]$: 378.20. Found: 377.14.

Synthesis of Compound 15a—Compound **14a** (0.5 g, 1.47 mmol) was added to a solution of EDAC (0.57g, 3.67 mmol) in DMF. The mixture was stirred at room temperature for 30 min after which DIPEA (1.28 mL, 7.35 mmol) and 3-(aminomethyl)pyridine, **3** (0.24g, 2.21 mmol) were added. The reaction was allowed to stir for 18 h. On completion, the solvent was evaporated and the reaction mixture was diluted with ethyl acetate. The organic layer was then washed with saturated $NaHCO_3$, water, and brine. The combined organic layers were dried over Na_2SO_4 and concentrated to give the crude product which was then purified using column chromatography (ethyl acetate/ methanol). The pure product **15a** was obtained as white solid in 62% yield (0.39 g). ^{l}H NMR ($CDC1_3$, 500 MHz) δ 8.54 (d, J = 14.4 Hz, 2H), 7.66 (d, J = 9.4 Hz, 1H), 7.31–7.16 (m, 6H), 6.69 (bs, 1H), 4.72 (d, J = 10.3 Hz, 1H), 4.52–4.40 (m, 2H), 2.87 (t, J = 9.3 Hz, 3H), 2.63–2.51 (m, 4H), 1.40 (d, J = 4.15 Hz, 2H), 1.36 (s, 9H); ^{13}C NMR ($CDCl_3$,125 MHz) δ 149.2, 148.8, 135.6, 129.4, 129.3, 128.8, 128.6, 126.7, 123.6, 41.0, 36.6, 28.6, 28.3. HRMS *m/z* calculated for $C_{23}H_{31}N_3O_3S$ $[M + H]^+$: 430.231. Found: 430.21.

The pure product **15b** was obtained as yellow oil in 56% yield. ^{1}H NMR ($CDCl_3$, 500 MHz) δ 8.51 (bs, 2H), 8.25 (s, 1H), 7.64 (d, J = 7.59 Hz, 2H), 7.35 (d, J = 8.07 Hz, 1H), 5.95 (bs, 1H), 7.23 (t, J = 4.85 Hz, 1H), 7.18 (t, J = 7.58 Hz, 1H), 7.11 (t, J = 7.28 Hz, 1H), 7.02 (s, 1H), 6.54 (s, 1H), 4.76 (bs, 1H), 4.41 (t, J = 5.91 Hz, 2H), 4.05 (m, 1H), 3.01 (bs, 2H), 2.86 (bm, 2H), 2.62 (bm, 2H), 2.49 (bm, 2H), 1.36 (s, 9H); ^{13}C NMR ($CDCl_3$,125 MHz) δ 155.7,149.1,148.7,136.3,135.7,134.1, 129.4, 126.6, 123.6, 122.9, 122.2, 119.7, 119.0, 111.3, 111.2, 50.7,41.0, 36.5, 35.8, 28.8, 28.4. HRMS *m/z* calculated for $C_{17}H_{27}N_3O_3$ $[M + Na]^+$: 491.21. Found: 491.2.

The purity of compounds **4, 5, 15a**, and **15b** was >95% as determined by ^{1}H NMR analysis. The purity of compound **11**, however, did not exceed 90% even after repeated attempts of column chromatography purification.

Protein Expression and Purification

The K282A/E285A mutation was introduced to the CYP3A4Δ3–22 expression plasmid using a QuikChange mutagenesis kit (Stratagene). The C-terminally 4-histidine tagged wild type and mutant CYP3A4 were produced, purified, and quantified as reported previously.[25]

Spectral Binding Titrations

Ligand binding to CYP3A4 was monitored in 50 mM phosphate, pH 7.4, containing 20% glycerol and **1** mM dithiothreitol (buffer A) in a Cary 300 spectrophotometer. The protein was titrated with small aliquots of the investigated compounds dissolved in dimethyl sulfoxide, with the final solvent concentration of <2%. Spectral dissociation constants (K_s) were determined from the titration curves using one- or two-site saturation fitting.

Kinetics of Ligand Binding

Kinetics of ligand binding to CYP3A4 was monitored at room temperature in 50 mM phosphate, pH 7.4, in a SX.18MV stopped flow apparatus (Applied Photophysics, U.K.) after mixing 2 μM CYP3A4 with various concentrations of ligands. Absorbance changes were followed at 409–411 nm for pyridine, aminoethylpyridine, and compound 5 and at 427–428 nm for **4, 11**, and **15a,b**. Kinetic data were analyzed using the program IgorPro (WaveMetrics, Inc.).

Thermal Denaturation and Inhibitory Potency Assays

Thermal denaturation experiments were conducted as previously described[27] to compare ligand-dependent changes in CYP3A4 stability. The inhibitory potency of the investigated compounds on the 7-benzyloxy-4-(trifluoromethyl)coumarin (BFC) O-debenzylation activity of CYP3A4 was evaluated fluorometrically in a reconstituted system with rat cytochrome P450 reductase (CPR). The reaction was carried out at room temperature in 100 mM phosphate buffer, pH 7.4, containing catalase and superoxide dismutase (2 units/mL each). A mixture of 1 μM CYP3A4 and 1 μM CPR was preincubated for 1 h at room temperature and diluted by 20-fold with the assay buffer immediately before measurements. BFC (50 μM), and various concentrations of analogs were added to the protein mixture 2 min prior to the reaction initiation with 100 μM NADPH. Formation of 7-hydroxy-4-

trifluoromethylcoumarin was followed in a Hitachi F100 fluorometer using λ_{ex} = 430 nm and λ_{em} = 500 nm. IC_{50} values were derived from the [% activity] vs [inhibitor] plots.

Crystallization and Determination of the X-ray Structures of Ligand-bound CYP3A4

CYP3A4 K282A/E285A was cocrystallized with **4** by a sitting drop vapor diffusion method. Protein (80 mg/mL) in buffer A was mixed with a 10-fold excess of **4** and centrifuged to remove the precipitate. CYP3A4 K282A/E285A directly ligated to **4** was crystallized against the 80% solution E7 from the Morpheus crystallization screen (Molecular Dimensions). The imidazole-contain-ing solution A3 from the same screening kit resulted in cocrystallization of the mutant with both imidazole and **4** in the active site. Crystals of the wild type CYP3A4 bound to compounds **15a** and **15b** were grown by a microbatch method under oil. A half of a microliter of ligand-bound CYP3A4 was mixed with 0.5 μL of 6–10% polyethylene glycol 3350 and 60–90 mM sodium malonate, pH 5.0, and covered with paraffin oil. All crystals were cryoprotected with Paratone-N and frozen in liquid nitrogen. X-ray diffraction data were collected at the Stanford Synchrotron Radiation Lightsource beamline 7-1 and the Advanced Light Source beamline 8.2.1. Crystal structures were solved by molecular replacement with PHASER[37] and the ligand-free 1TQN structure as a search model. The initial models were rebuilt and refined with COOT,[38] PHENIX,[39] and REFMAC.[37] Data collection and refinement statistics are summarized in the Supporting Information Table 1S. The atomic coordinates and structure factors for **4**-, imidazole/**4**-, **15a**-, and **15b**-bound CYP3A4 have been deposited in the Protein Data Bank with the codes 4D75, 4D6Z, 4D78, and 4D7D, respectively.

Supplementary Material

Refer to Web version on PubMed Central for supplementary material.

Acknowledgments

This work was supported by the NIH National Institute of General Medical Sciences (Grant GM57353, T.L.P.) and the University of California's Center for Antiviral Drug Discovery (Grant MRPI1443226, A.R.C. and T.L.P.) and involves research carried out at the Advanced Light Source and the Stanford Synchrotron Radiation Lightsource, a national user facility operated by Stanford University on behalf of the U.S. Department of Energy, Office of Basic Energy Sciences. The Advanced Light Source is supported by the Director, Office of Science, Office of Basic Energy Sciences, of the U.S. Department of Energy under Contract DE-AC0205CH11231. The SSRL Structural Molecular Biology Program is supported by the Department of Energy, Office of Biological and Environmental Research, and by National Institutes of Health, National Center for Research Resources, Biomedical and Technology Program, and the National Institute of General Medical Sciences. The authors also thank J. Milligan and M. Vasquez for technical assistance.

ABBREVIATIONS USED

CYP3A4	3A4 isoform of cytochrome P450
CPR	cytochrome P450 reductase
BFC	7-benzyloxy-4-(trifluoromethyl)coumarin

REFERENCES

1. Guengerich FP, Shimada T. Oxidation of toxic and carcinogenic chemicals by human cytochrome P-450 enzymes. Chem. Res. Toxicol. 1991; 4:391–407. [PubMed: 1912325]
2. Li AP, Kaminski DL, Rasmussen A. Substrates of human hepatic cytochrome P450 3A4. Toxicology. 1995; 104:1–8. [PubMed: 8560487]
3. Guengerich FP. Cytochrome P-450 3A4: regulation and role in drug metabolism. Annu. Rev. Pharmacol. Toxicol. 1999; 39:1–17. [PubMed: 10331074]
4. Mehmood Z, Kelly DE, Kelly SL. Cytochrome P450 3A4 mediated metabolism of 2,4-dichlorophenol. Chemosphere. 1997; 34:2281–2291. [PubMed: 9192464]
5. Chae YH, Yun CH, Guengerich FP, Kadlubar FF, el-Bayoumy K. Roles of human hepatic and pulmonary cytochrome P450 enzymes in the metabolism of the environmental carcinogen 6-nitrochrysene. Cancer. Res. 1993; 53:2028–2034. [PubMed: 8481905]
6. Hodgson E. In vitro human phase I metabolism of xenobiotics I: pesticides and related compounds used in agriculture and public health. J. Biochem. Mol. Toxicol. 2003; 17:201–206. [PubMed: 12898643]
7. Mehmood Z, Williamson MP, Kelly DE, Kelly SL. Human cytochrome P450 3A4 is involved in the biotransformation of the herbicide 2,4-dichlorophenoxyacetic acid. Environ. Toxicol. Pharmacol. 1996; 2:397–401. [PubMed: 21781748]
8. Mehmood Z, Williamson MP, Kelly DE, Kelly SL. Metabolism of organochlorine pesticides: the role of human cytochrome P450 3A4. Chemosphere. 1996; 33:759–769. [PubMed: 8759309]
9. Kempf DJ, Marsh KC, Kumar G, Rodrigues AD, Denissen JF, McDonald E, Kukulka MJ, Hsu A, Granneman GR, Baroldi PA, Sun E, Pizzuti D, Plattner JJ, Norbeck DW, Leonard JM. Pharmacokinetic enhancement of inhibitors of the human immunodeficiency virus protease by coadministration with ritonavir. Antimicrob. Agents Chemother. 1997; 41:654–660. [PubMed: 9056009]
10. Xu L, Desai MC. Pharmacokinetic enhancers for HIV drugs. Curr. Opin. Invest. Drugs. 2009; 10:775–786.
11. Mathias AA, German P, Murray BP, Wei L, Jain A, West S, Warren D, Hui J, Kearney BP. Pharmacokinetics and pharmacodynamics of GS-9350: a novel pharmacokinetic enhancer without anti-HIV activity. Clin. Pharmacol. Ther. 2010; 87:322–329. [PubMed: 20043009]
12. Xu L, Liu H, Murray B, Callebaut C, Lee MS, Hong A, Strickley RG, Tsai LK, Stray KM, Wang Y, Rhodes GR, Desai MC. Cobicistat (GS-9350): A potent and selective inhibitor of human CYP3A as a novel pharmacoenhancer. ACS Med. Chem. Lett. 2010; 1:209–213. [PubMed: 24900196]
13. Xu L, Liu H, Hong A, Vivian R, Murray BP, Callebaut C, Choi YC, Lee MS, Chau J, Tsai LK, Stray KM, Strickley RG, Wang J, Tong L, Swaminathan S, Rhodes GR, Desai MC. Structure-activity relationships of diamine inhibitors of cytochrome P450 (CYP) 3A as novel pharmacoenhancers. Part II: P2/P3 region and discovery of cobicistat (GS-9350). Bioorg. Med. Chem. Lett. 2014; 24:995–999. [PubMed: 24412072]
14. Kempf DJ, Marsh KC, Denissen JF, McDonald E, Vasavanonda S, Flentge CA, Green BE, Fino L, Park CH, Kong XP, et al. ABT-538 is a potent inhibitor of human immunodeficiency virus protease and has high oral bioavailability in humans. Proc. Natl. Acad. Sci. U. S. A. 1995; 92:2484–2488. [PubMed: 7708670]
15. Koudriakova T, Iatsimirskaia E, Utkin I, Gangl E, Vouros P, Storozhuk E, Orza D, Marinina J, Gerber N. Metabolism of the human immunodeficiency virus protease inhibitors indinavir and ritonavir by human intestinal microsomes and expressed cytochrome P4503A4/3A5: mechanism-based inactivation of cytochrome P4503A by ritonavir. Drug Metab. Dispos. 1998; 26:552–561. [PubMed: 9616191]
16. von Moltke LL, Durol AL, Duan SX, Greenblatt DJ. Potent mechanism-based inhibition of human CYP3A in vitro by amprenavir and ritonavir: comparison with ketoconazole. Eur. J. Clin. Pharmacol. 2000; 56:259–261. [PubMed: 10952482]
17. Ernest CS 2nd, Hall SD, Jones DR. Mechanism-based inactivation of CYP3A by HIV protease inhibitors. J. Pharmacol. Exp. Ther. 2005; 312:583–591. [PubMed: 15523003]

18. Lin HL, D'Agostino J, Kenaan C, Calinski D, Hollenberg PF. The effect of ritonavir on human CYP2B6 catalytic activity: heme modification contributes to the mechanism-based inactivation of CYP2B6 and CYP3A4 by ritonavir. Drug Metab. Dispos. 2013; 41:1813–1824. [PubMed: 23886699]
19. Rock BM, Hengel SM, Rock DA, Wienkers LC, Kunze KL. Characterization of Ritonavir-Mediated Inactivation of Cytochrome P450 3A4. Mol. Pharmacol. 2014; 86:665–674. [PubMed: 25274602]
20. Sekiguchi N, Higashida A, Kato M, Nabuchi Y, Mitsui T, Takanashi K, Aso Y, Ishigai M. Prediction of drug-drug interactions based on time-dependent inhibition from high throughput screening of cytochrome P450 3A4 inhibition. Drug Metab. Pharmacokinet. 2009; 24:500–510. [PubMed: 20045985]
21. Iribarne C, Berthou F, Carlhant D, Dreano Y, Picart D, Lohezic F, Riche C. Inhibition of methadone and buprenorphine N-dealkylations by three HIV-1 protease inhibitors. Drug Metab. Dispos. 1998; 26:257–260. [PubMed: 9492389]
22. Eagling VA, Back DJ, Barry MG. Differential inhibition of cytochrome P450 isoforms by the protease inhibitors, ritonavir, saquinavir and indinavir. Br. J. Clin. Pharmacol. 1997; 44:190–194. [PubMed: 9278209]
23. Kumar GN, Rodrigues AD, Buko AM, Denissen JF. Cytochrome P450-mediated metabolism of the HIV-1 protease inhibitor ritonavir (ABT-538) in human liver microsomes. J. Pharmacol. Exp. Ther. 1996; 277:423–431. [PubMed: 8613951]
24. Zalma A, von Moltke LL, Granda BW, Harmatz JS, Shader RI, Greenblatt DJ. In vitro metabolism of trazodone by CYP3A: inhibition by ketoconazole and human immunodeficiency viral protease inhibitors. Biol. Psychiatry. 2000; 47:655–661. [PubMed: 10745059]
25. Sevrioukova IF, Poulos TL. Structure and mechanism of the complex between cytochrome P4503A4 and ritonavir. Proc. Natl. Acad. Sci. U. S. A. 2010; 107:18422–18427. [PubMed: 20937904]
26. Sevrioukova IF, Poulos TL. Interaction of human cytochrome P4503A4 with ritonavir analogs. Arch. Biochem. Biophys. 2012; 520:108–116. [PubMed: 22410611]
27. Sevrioukova IF, Poulos TL. Pyridine-substituted desoxy-ritonavir is a more potent cytochrome P450 3A4 inhibitor than ritonavir. J. Med. Chem. 2013; 56:3733–3741. [PubMed: 23586711]
28. Sevrioukova IF, Poulos TL. Dissecting cytochrome P450 3A4-ligand interactions using ritonavir analogues. Biochemistry. 2013; 52:4474–4481. [PubMed: 23746300]
29. Sevrioukova IF, Poulos TL. Ritonavir analogues as a probe for deciphering the cytochrome P450 3A4 inhibitory mechanism. Curr. Top. Med. Chem. 2014; 14:1348–1355. [PubMed: 24805065]
30. Ekins S, Bravi G, Binkley S, Gillespie JS, Ring BJ, Wikel JH, Wrighton SA. Three- and four-dimensional quantitative structure activity relationship analyses of cytochrome P-450 3A4 inhibitors. J. Pharmacol. Exp. Ther. 1999; 290:429–438. [PubMed: 10381809]
31. Ekins S, Bravi G, Wikel JH, Wrighton SA. Three-dimensional-quantitative structure activity relationship analysis of cytochrome P-450 3A4 substrates. J. Pharmacol. Exp. Ther. 1999; 291:424–433. [PubMed: 10490933]
32. Ekins S, Stresser DM, Williams JA. In vitro and pharmacophore insights into CYP3A enzymes. Trends Pharmacol. Sci. 2003; 24:161–166. [PubMed: 12707001]
33. Riley RJ, Parker AJ, Trigg S, Manners CN. Development of a generalized, quantitative physicochemical model of CYP3A4 inhibition for use in early drug discovery. Pharm. Res. 2001; 18:652–655. [PubMed: 11465421]
34. Liu H, Xu L, Hui H, Vivian R, Callebaut C, Murray BP, Hong A, Lee MS, Tsai LK, Chau JK, Stray KM, Cannizzaro C, Choi YC, Rhodes GR, Desai MC. Structure-activity relationships of diamine inhibitors of cytochrome P450 (CYP) 3A as novel pharmacoenhancers, part I: core region. Bioorg. Med. Chem. Lett. 2014; 24:989–994. [PubMed: 24411125]
35. Goldschmidt L, Cooper DR, Derewenda ZS, Eisenberg D. Toward rational protein crystallization: A Web server for the design of crystallizable protein variants. Protein Sci. 2007; 16:1569–1576. [PubMed: 17656576]

36. Williams PA, Cosme J, Vinkovic DM, Ward A, Angove HC, Day PJ, Vonrhein C, Tickle IJ, Jhoti H. Crystal structures of human cytochrome P450 3A4 bound to metyrapone and progesterone. Science. 2004; 305:683–686. [PubMed: 15256616]

37. CCP4. Collaborative computational project number 4. The CCP4 suite programs for protein crystallography. Acta Crystallogr. Sect. D: Biol. Crystallogr. 1994; 50:760–763.

38. Emsley P, Lohkamp B, Scott WG, Cowtan K. Features and development of Coot. Acta Crystallogr. Sect. D: Biol. Crystallogr. 2010; 66:486–501. [PubMed: 20383002]

39. Adams PD, Afonine PV, Bunkoczi G, Chen VB, Davis IW, Echols N, Headd JJ, Hung LW, Kapral GJ, Grosse-Kunstleve RW, McCoy AJ, Moriarty NW, Oeffner R, Read RJ, Richardson DC, Richardson JS, Terwilliger TC, Zwart PH. PHENIX: a comprehensive Python-based system for macromolecular structure solution. Acta Crystallogr., Sect. D: Biol. Crystallogr. 2010; 66:213–221. [PubMed: 20124702]

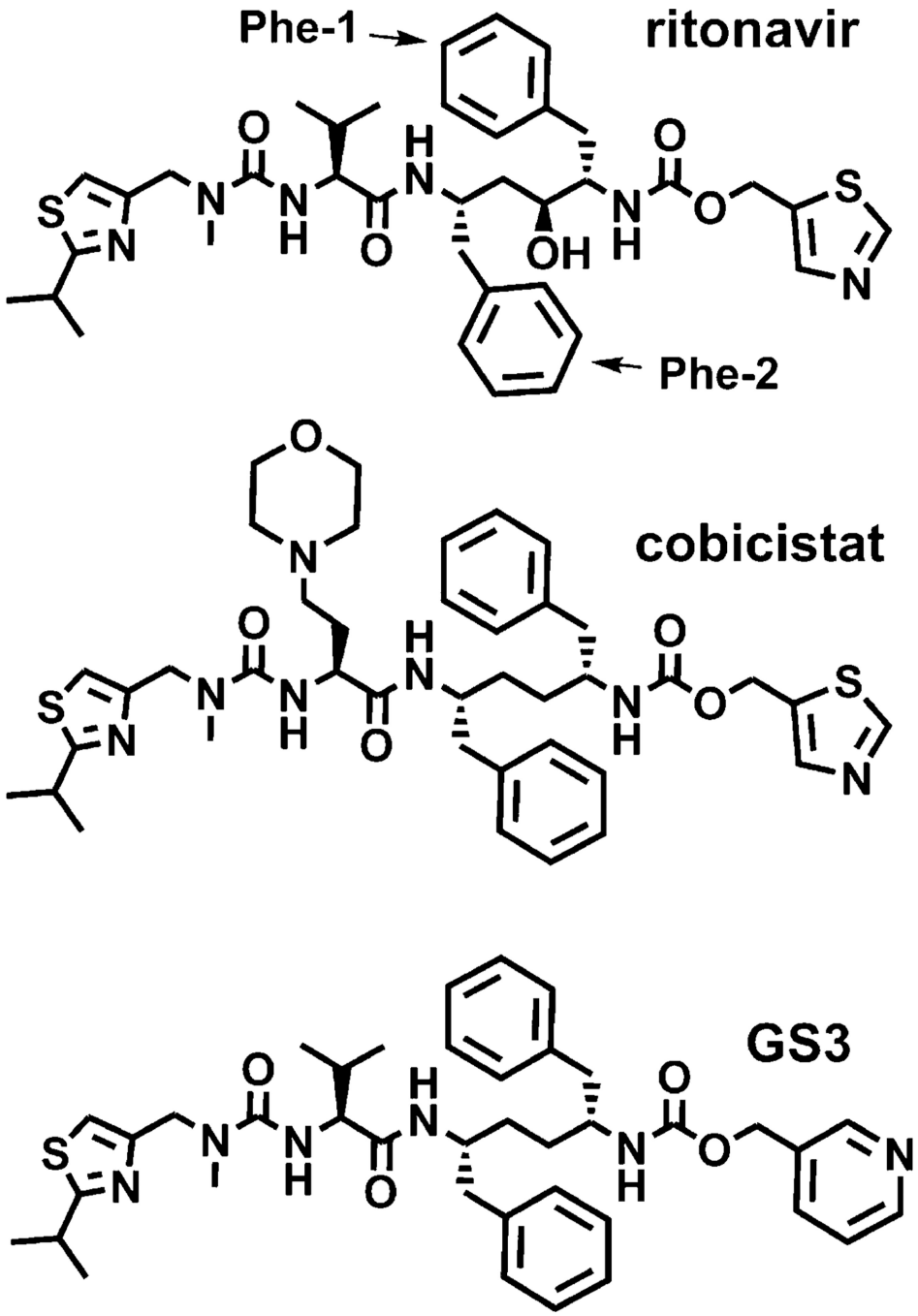

Figure 1.

Chemical structures of ritonavir, cobicistat, and GS3. The phenyl side groups proximal and distant from the heme-ligating moiety are designated as Phe-1 and Phe-2, respectively.

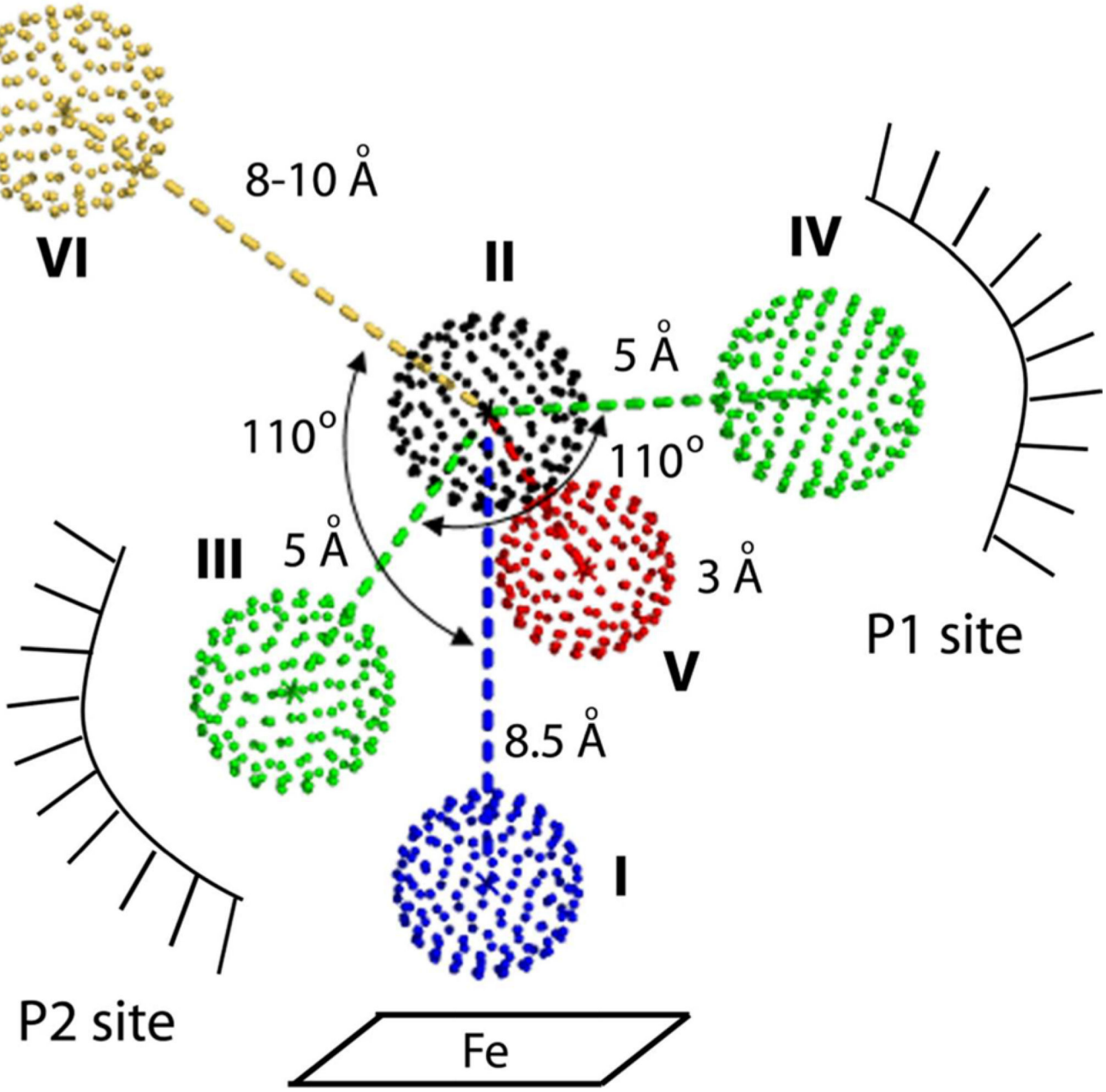

Figure 2.

Pharmacophore model for a CYP3A4-specific inhibitor derived from the structure/function studies on analogues of ritonavir. Pharmacophoric determinants are the following: I, strong heme-ligating nitrogen donor; II, flexible backbone; III and IV, aromatic and hydrophobic moieties, respectively; V, hydrogen donor/acceptor; IV, polyfunctional end-group. The P1 and P2 sites are hydrophobic pockets adjacent to the phenylalanine cluster and the heme, respectively.

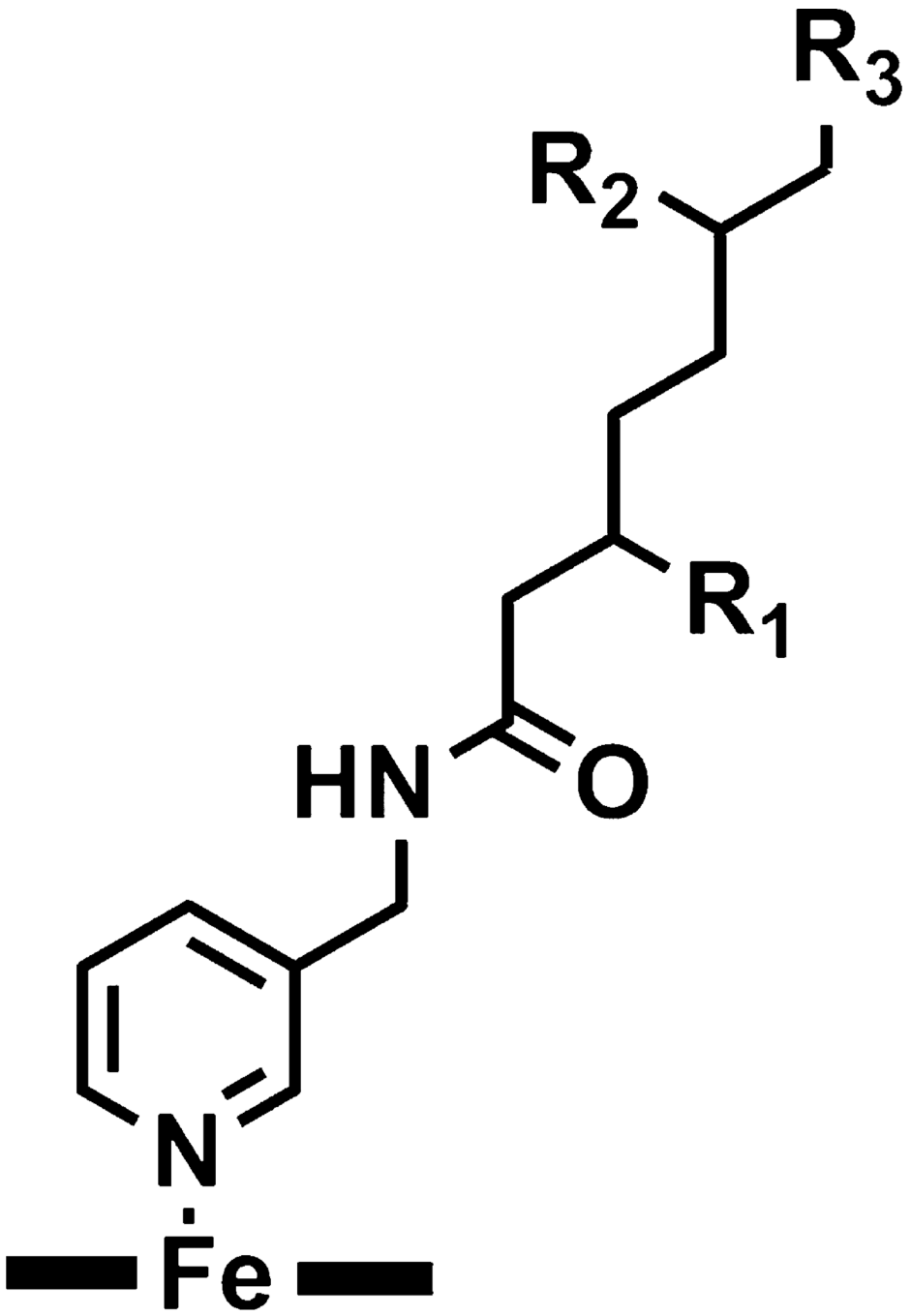

Figure 3.

Scaffold used for the CYP3A4 inhibitor design. The pyridine ring, serving as a heme-ligating moiety, is attached to a flexible backbone via a peptide bond, an H-donor/acceptor. By varying the side (R_1 and R_2) and terminal (R_3) groups, the role of each moiety in the CYP3A4 binding and inhibition can be probed.

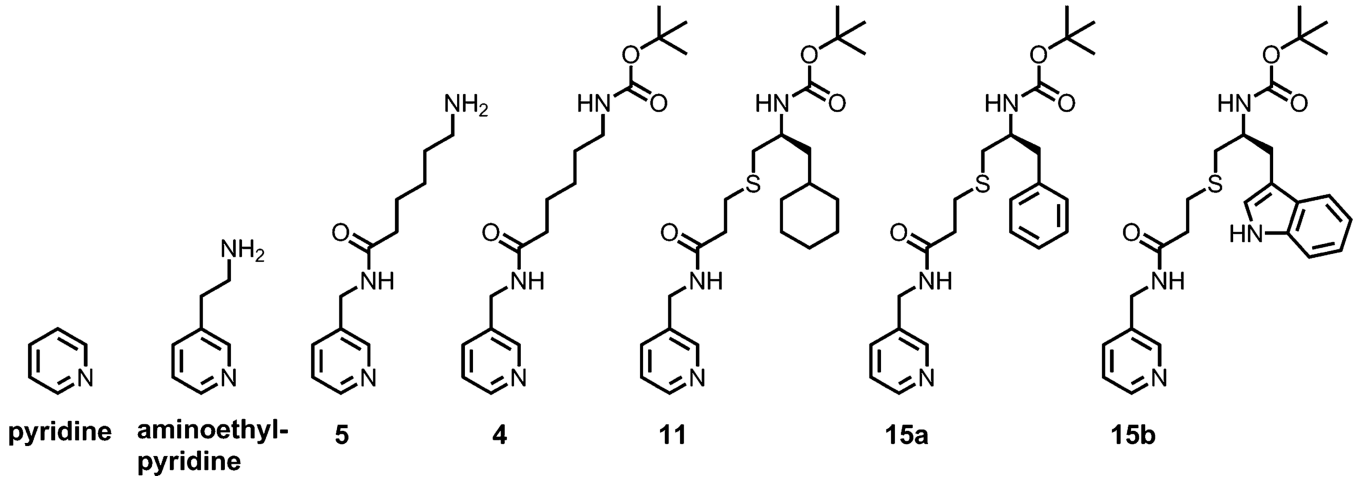

Figure 4.
Chemical structures of the investigated compounds.

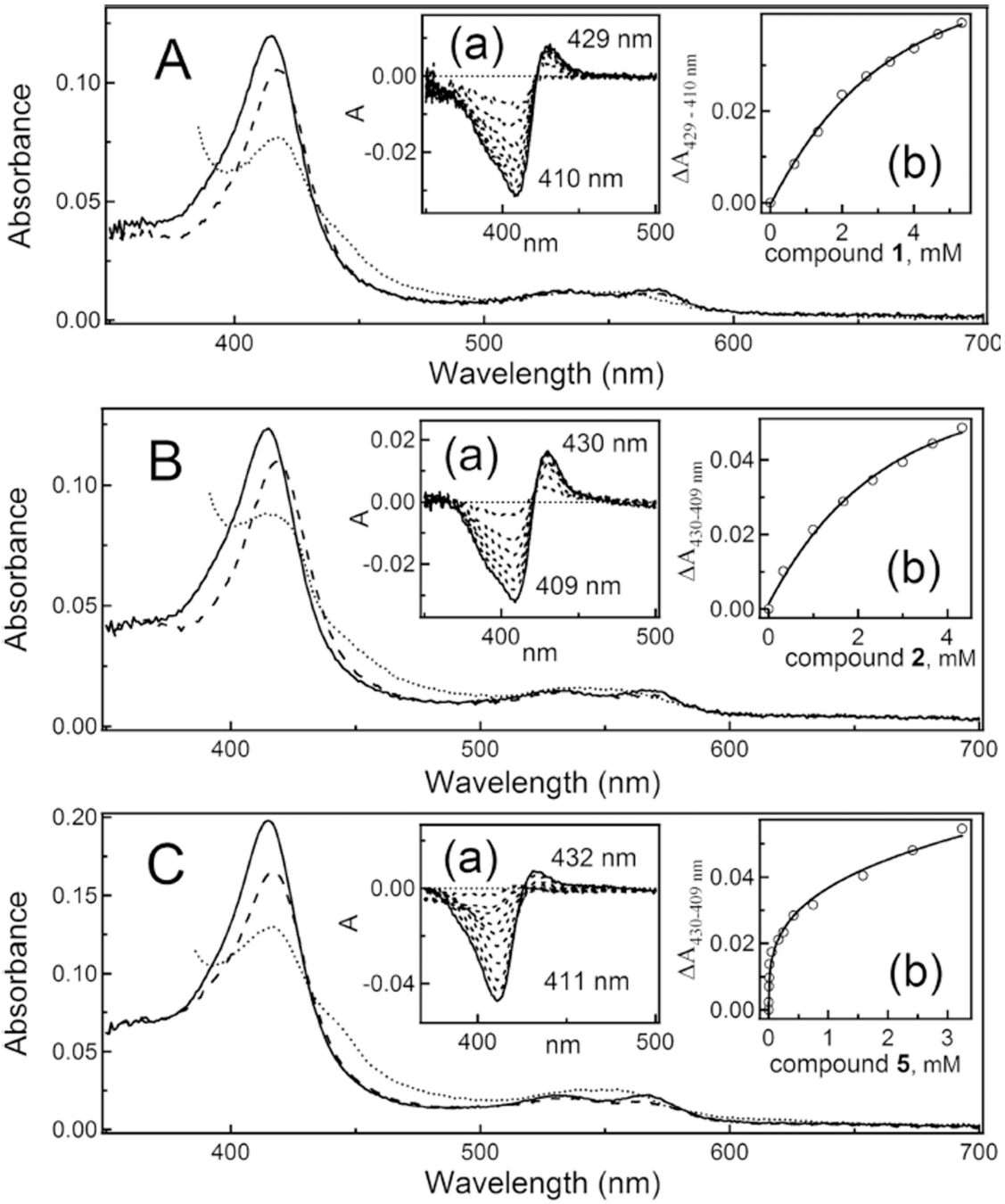

Figure 5.

(A–C) Spectral changes induced in CYP3A4 by pyridine, aminoethylpyridine, and compound **5**, respectively. Absorbance spectra of the ferric ligand-free, ligand-bound, and ferrous ligand-bound forms are shown in solid, dashed, and dotted lines, respectively. Insets (a) are absorbance changes observed during equilibrium titration of CYP3A4 with pyridine, aminoethylpyridine and **5**. Insets (*b*) are plots of absorbance change vs ligand concentration.

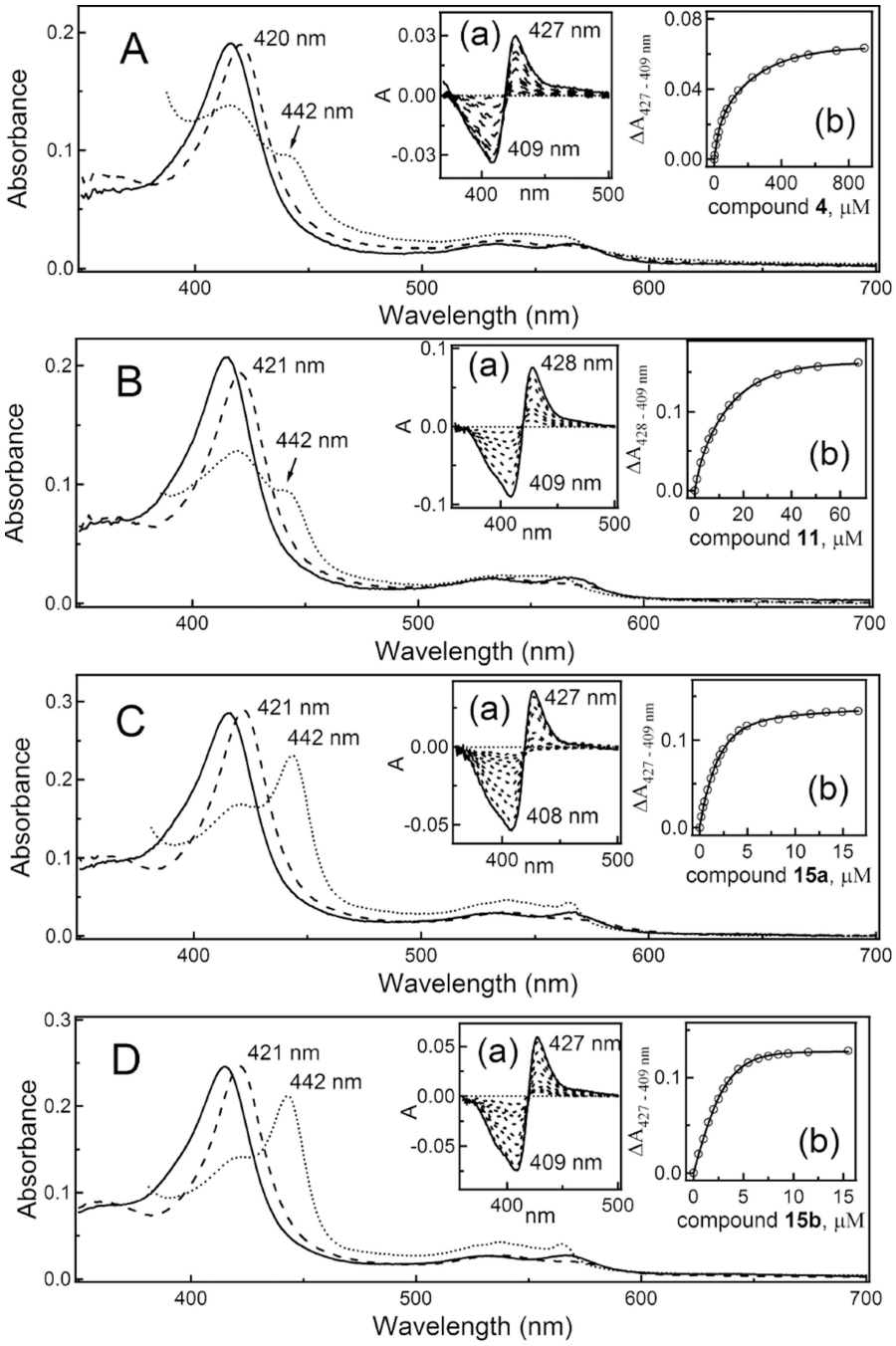

Figure 6.

(A–D) Spectral changes induced in CYP3A4 by compounds **4, 11, 15a**, and **15b**, respectively. Absorbance spectra of the ferric ligand-free, ligand-bound, and ferrous ligand-bound forms are shown in solid, dashed, and dotted lines, respectively. Absorbance maxima of the ferric and ferrous ligand-bound CYP3A4 are indicated. Insets (a) are absorbance changes observed during equilibrium titration of CYP3A4 with **4, 11**, and **15a,b**. Insets (b) are plots of absorbance change vs ligand concentration.

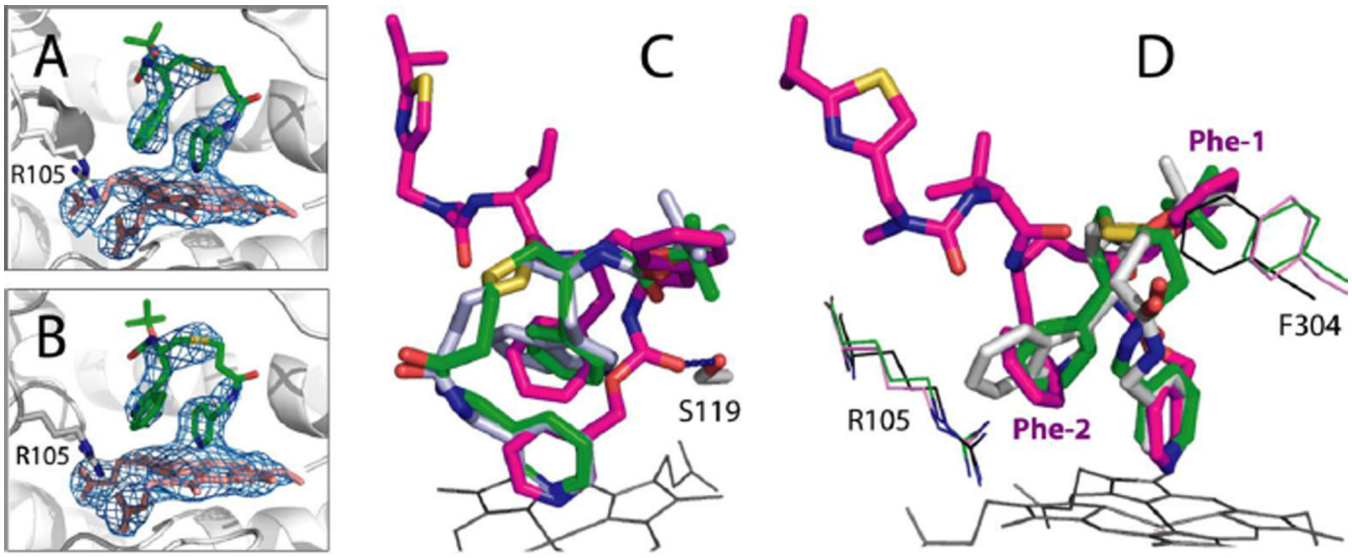

Figure 7.

(A, B) Active site of CYP3A4 bound to compounds **15a** and **15b**, respectively. The ligands (in green), heme (in pink), and the Arg105 side group are shown in stick representation. $2F_o - F_c$ electron density maps are contoured at 1σ. (C, D) Relative orientation of **15a** (green), **15b** (light gray), and GS3 (magenta). Panel C shows that a 180° rotation of **15a** and **15b** relative to GS3 prevents H-bond formation with Ser119. Panel D demonstrates that the Boc groups of **15a** and **15b** occupy the P1 site and displace the I-helix Phe304 to the same extent as GS3 Phe-1 does.

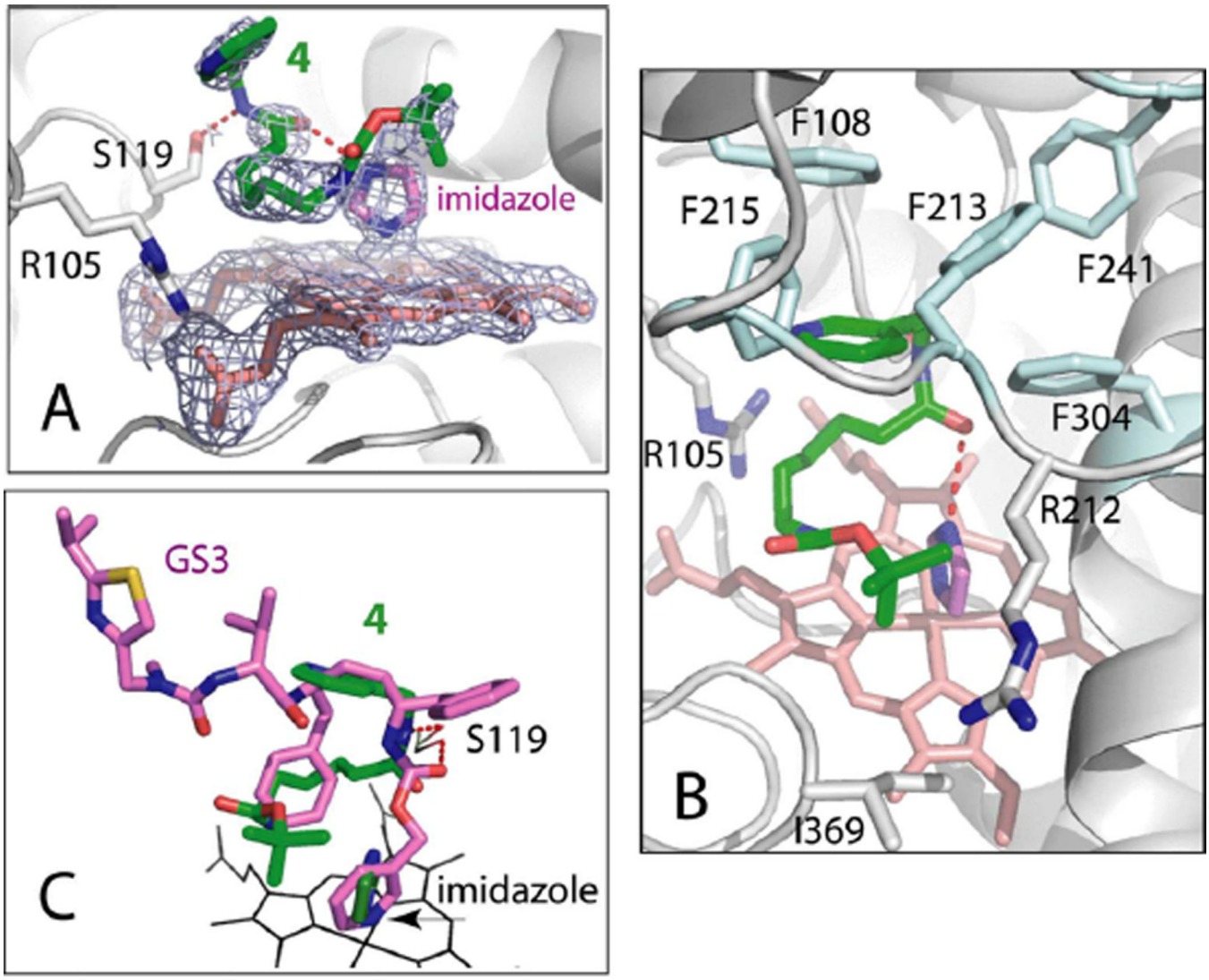

Figure 8.

The 1.93 Å crystal structure of CYP3A4 K282A/E285A bound to **4** and imidazole. (A) Imidazole (in magenta) ligates to the heme, whereas compound **4** binds nearby. The complex is stabilized by two hydrogen bonds (depicted as red dotted lines) established between the carbonyl oxygen and amide nitrogen of **4** and the imidazole nitrogen and Ser119 hydroxyl group, respectively. $2F_o - F_c$ electron density map is contoured at 1σ. (B) Another view at the active site showing how the pyridine ring of **4** is positioned relative to the phenylalanine cluster (residues 108, 213, 215, 241, and 304). (C) Superposition of the **4**- and GS3-bound structures (in green and magenta, respectively). H-bonds to Ser119 are shown as red dotted lines.

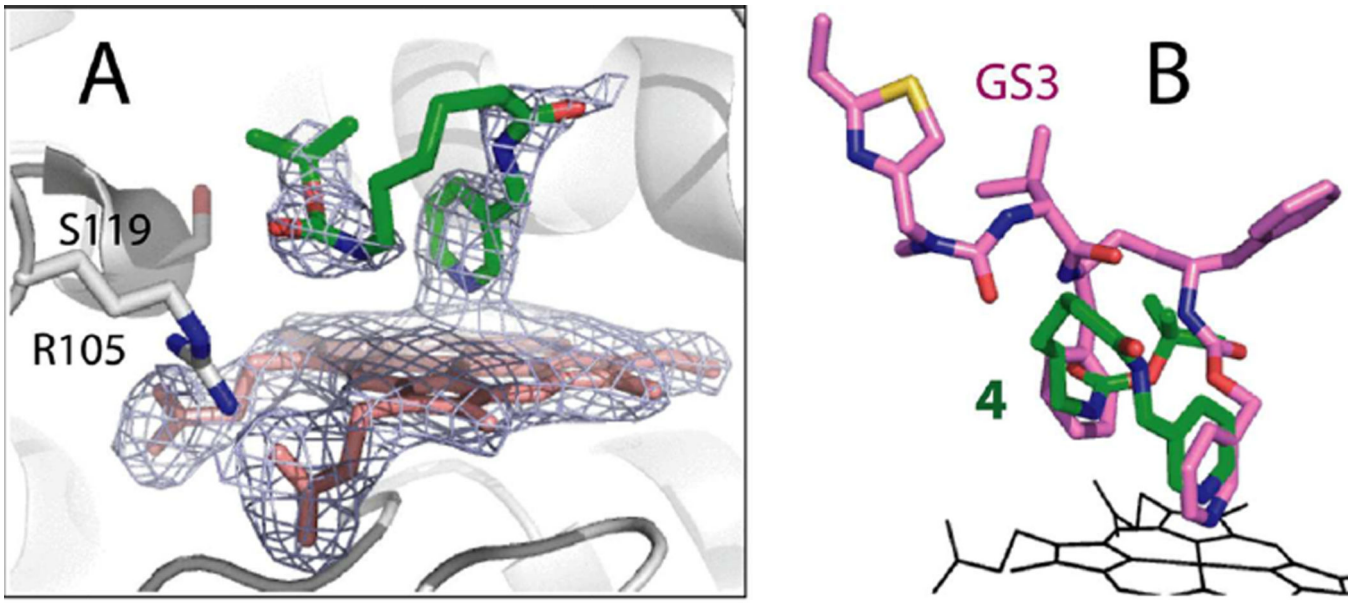

Figure 9.

The 2.25 Å crystal structure of CYP3A4 K282A/E285Aligated to **4**. (A) Compound **4** directly binds to the heme via the pyridine nitrogen. The **4** backbone bends in order to place the end portion into the P2 site. $2F_o - F_c$ electron density map is contoured at 1σ. (B) Superposition of the **4**- and GS3-bound structures reveals that, similar to **15a** and **15b**, compound **4** rotates around the pyridine nitrogen by ~180° to optimize hydrophobic interactions at the P2 site through the aliphatic backbone and Boc moiety.

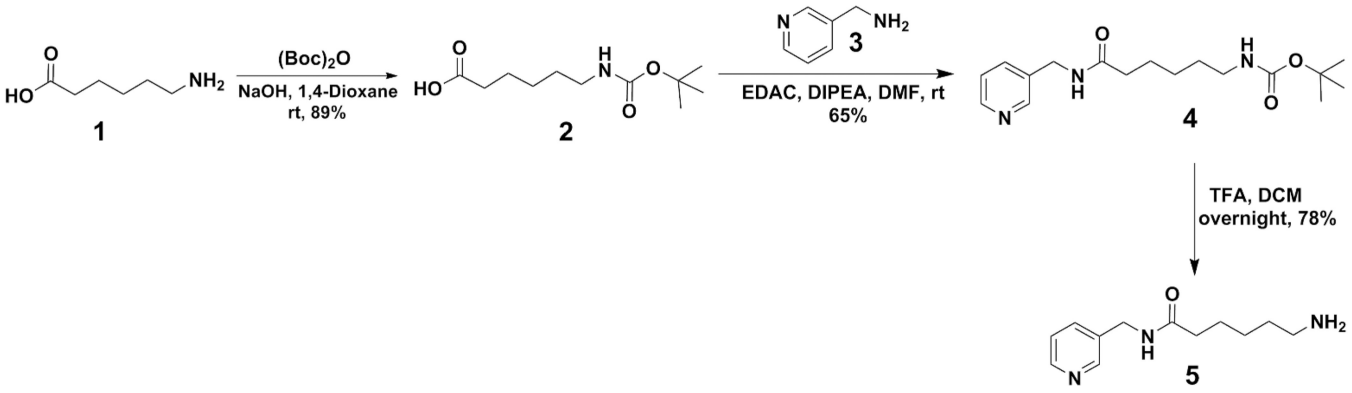

Scheme 1.

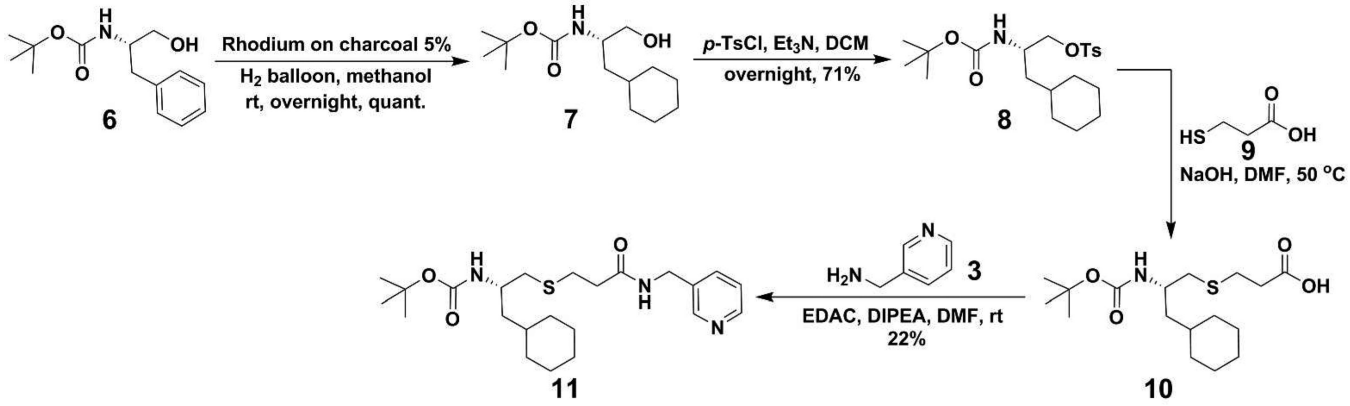

Scheme 2.

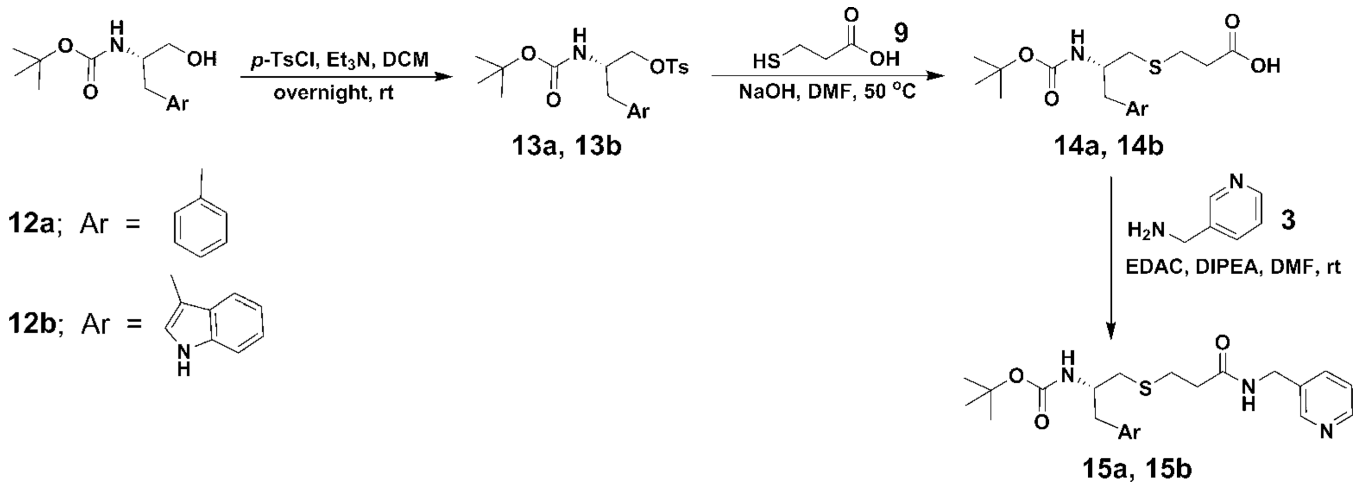

Scheme 3.

Table 1

Properties of Pyridine-Containing Compounds

	442 nm band[a] (Fe^{2+})	K_s[b] (μM)	k_{fast}[c] (s^{-1})	ΔT_m[d] (°C)	IC_{50}[e] (μM)
pyridine	−	4500 ± 400	0.5 ± 0.1	0	4000 ± 500
aminoethylpyridine	−	2500 ± 200	0.6 ± 0.1	−0.1	5000 ± 600
5	−	10 ± 1[f] 4400 ± 500[f]	0.8 ± 0.1	−0.2	1000 ± 150
4	+	105 ± 10	20 ± 2	−0.2	75 ± 5
11	+	10 ± 1	4.0 ± 0.2	−2 ± 0.4	30 ± 3
15a	++	0.9 ± 0.1	1.7 ± 0.2	−1 ± 0.2	0.52 ± 0.05
15b	++	0.5 ± 0.1	8.0 ± 1.5	0.2	0.21 ± 0.04
GS3[g]	+++	0.025	7.0	5.1	0.13
ritonavir[g]	+++	0.051	1.4	2.7	0.55

[a] Appearance and magnitude of the 442 nm peak in the absorbance spectrum of ligand-bound ferrous CYP3A4.

[b] Spectral dissociation constant.

[c] Rate constant for the fast phase of the binding reaction measured at saturating ligand concentrations.

[d] Ligand-dependent changes in the melting temperature of CYP3A4. eConcentration required for half-maximal inactivation of recombinant CYP3A4.

[f] Values derived from the two-site saturation fit to a titration curve.

[g] Determined previously.[25,27]

J Med Chem. Author manuscript; available in PMC 2016 August 25.

Table 2

High Entropy Residues in CYP3A4 Identified by a Surface Entropy Reduction Prediction (SERp) Server (http://services.mbi.ucla.edu/SER/)

cluster	residue	$SER_{p\ score}$ [a]	proposed mutation
1	^{421}KKNK^{424}	6.51	K421A/K422A/K424A
2	^{282}KETESHKA^{289}	6.3	K282A/E263A/E285A
3	^{469}KETQ^{472}	5.26	K469A/E470A
4	^{486}EK^{487}	5.09	E486A/K487A
5	^{378}KKDVE^{382}	5.07	K378A/K379A

[a]The highest score is assigned to a cluster with the highest probability to enhance crystallizability upon mutation.